Journal of Power Sources 194 (2009) 854–863

Contents lists available at ScienceDirect

Journal of Power Sources

journal homepage: www.elsevier.com/locate/jpowsour

Three-dimensional modeling of planar solid oxide fuel cells and the rib design optimization

Shixue Liu[a,b,c,d], Wei Kong[b], Zijing Lin[a,b,*]

[a] Hefei National Laboratory for Physical Sciences at the Microscale, University of Science and Technology of China, Hefei 230026, China
[b] Department of Physics, University of Science and Technology of China, Hefei 230026, China
[c] Qingdao Institute of Bioenergy and Bioprocess Technology, Chinese Academy of Sciences, Qingdao 266101, China
[d] Key Laboratory of Biofuels, Chinese Academy of Sciences, Qingdao 266101, China

ARTICLE INFO

Article history:
Received 18 May 2009
Received in revised form 17 June 2009
Accepted 17 June 2009
Available online 24 June 2009

Keywords:
Solid oxide fuel cell
Three dimensional
Interconnect rib
Contact resistance
Design optimization

ABSTRACT

Three-dimensional (3D) multi-physics models of co-, counter- and cross-flow planar solid oxide fuel cell (SOFC) stack units are described. The models consider electronic conduction in the electrodes, ionic conduction in the electrolyte, mass transport in the porous electrodes and electrochemical reactions on the three phase boundaries. Based on the analysis of the ionic conducting equation for the thin electrolyte layer, a mathematically equivalent method is proposed to scale the electrolyte thickness with the corresponding change in the ionic conductivity to moderate the thin film effect in the meshing step and decrease the total number of degrees of freedom in the 3D numerical models. Examples of applications are given with typical physical fields illustrated and the characteristic features discussed for co-, counter- and cross-flow designs. The 3D models are also used to optimize the rib widths in SOFC stacks as a function of interconnect–electrode contact resistance.

1. Introduction

Anode-supported planar solid oxide fuel cell (SOFC) has received much attention in recent years due to its satisfactory power density at the intermediate temperature [1–4]. The reduced operation temperature of planar SOFC also enables cheaper materials to be used as interconnects and seals and increases the operation life that are vital for commercial applications [2,5]. To speed up the technology development, there have been a growing number of theory and modeling activities in this subject that provide in-depth insights to the research community.

As summarized in a few recent papers [6–12], numerical models of varying degrees of sophistication have been developed. Broadly speaking, these numerical models may be classified as micro-modeling [13–15], macro-modeling [8,12,16,17], and multi-scale modeling [18]. Micro-modeling focuses on the properties of new material systems and membrane–electrode assembly (MEA) and is particularly helpful in revealing the connection between the microstructures and the properties of the electrode materials, but is usually incapable of providing detailed information such as the distributions of current and gas species in a cell scale and the overall power densities of SOFC stacks in practical applications. Macro-modeling aims to predict the SOFC performance at the cell and stack level and is very useful for improving engineering designs, but is often limited by the experimentally determined model parameters and does not pursue the prediction of the fuel cell performances with different electrode microstructures. Multi-scale modeling in principle combines the advantages of both micro-modeling and macro-modeling, but is still in its infancy and integrated three-dimensional (3D) models are yet to appear. In fact, most macro-models are not truly 3D even if they appear to be. For example, the 3D modeling at the cell and stack scale reported in Refs. [16,17] assumed implicitly straight line paths for the current conduction and gas transport in MEA consisting of anode, electrolyte and cathode layers and should be regarded as quasi-3D models. Moreover, these models as well as most other models ignore issues in the stack assembly such as the effects of interconnect ribs on the performance of planar SOFCs [14,19–21]. Inclusion of the rib effects in cell- and stack-level models is critically important for the model predicting power as both the experiment and theory have shown that the performance degradation from ideal SOFC single cell to stack cell is very significant [19–23].

In the present work, multi-physics 3D numerical models coupling the mass transports in the porous electrodes, the electric current conduction in the MEA, and the electrochemical reactions at the gas–electrode–electrolyte three-phase boundary (TPB) are

* Corresponding author at: Hefei National Laboratory for Physical Sciences at the Microscale, University of Science and Technology of China, Hefei 230026, China. Tel.: +86 551 3606345; fax: +86 551 3606348.
E-mail address: zjlin@ustc.edu.cn (Z. Lin).

0378-7753/$ – see front matter © 2009 Elsevier B.V. All rights reserved.
doi:10.1016/j.jpowsour.2009.06.056

described. The current conduction in MEA is described by the partial differential equations for the electronic conduction in the electrodes and ionic conduction in the electrolyte. The dusty gas model is used to describe the mass transport process in the porous electrodes. The electrochemical reaction at the TPB is treated by the Butler–Volmer equation with the experimentally determined parameters. The models use realistic geometries of SOFC cells in practical applications and consider the co-, counter- and cross-flow designs in a stack assembly as well as take the effects of interconnect ribs on the gas transport and current conduction into consideration. An equivalent numerical method that is mathematically rigorous is proposed to reduce the mesh node numbers and enhance the efficiency of numerical simulation. As examples of applications, the models are used to simulate the stack cell performance and to optimize the rib design for the co-flow, counter-flow and cross-flow SOFC stacks.

2. Methods

2.1. Physical model

A planar SOFC stack is composed of repeating single fuel cells connected in series. In addition to the core part of a MEA with porous anode, dense electrolyte and porous cathode layers, another important component of a stack cell is the interconnect with parallel channels dug in both sides to distribute the gas flow across the cell. Examples of a repeating single cell with typical channel designs are shown in Fig. 1. Close-up views of the cell structures are illustrated in Fig. 2. The typical material, geometric and operational parameters are shown in Table 1. As shown in Table 1, the fuel cell model is assumed to be isothermal and all physical properties are determined at the temperature of 700 °C. Admittedly the material properties such as the electrolyte conductivity and the activation polarization are strongly influenced by the temperature field in a working SOFC stack [16,17]. However, we are leaving the model with coupled thermal conduction equations to a future development. Therefore, the modeling results here may be viewed as the baseline scenario when the temperature distributions are approximately uniform. Nevertheless, the following mathematical descriptions are formulated to be also applicable to non-isothermal cells if coupled with the thermal conduction equations. Moreover, the modeling results for the interconnect rib designs are expected to be valid also for non-isothermal SOFC stacks as the dominating physics is the competition between the current collection by the interconnect ribs and the gas transport in electrodes that are not very sensitive to the temperature field.

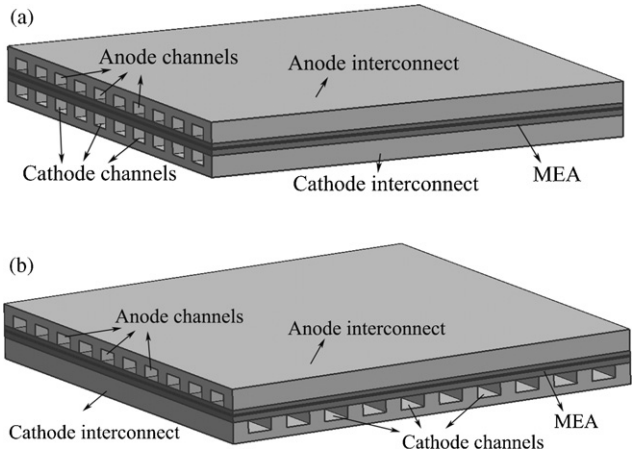

Fig. 1. Single cell unit of a planar SOFC stack: (a) co- or counter-flow; (b) cross-flow.

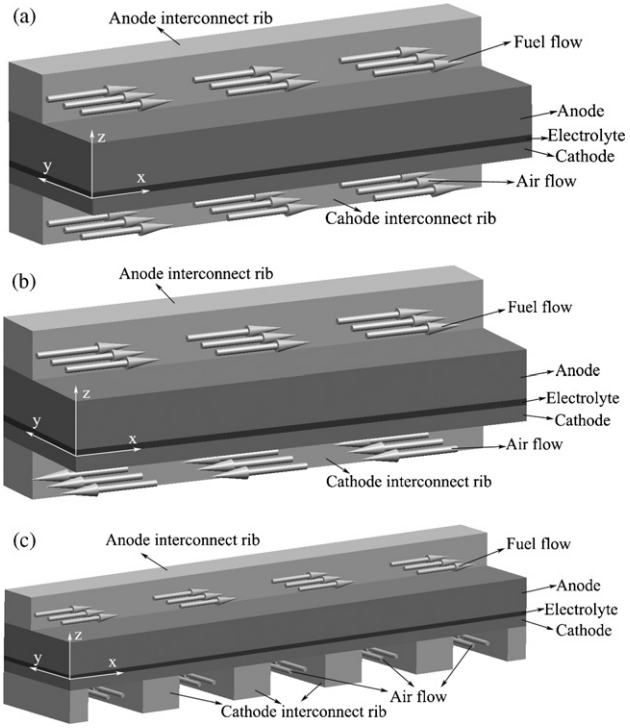

Fig. 2. Schematics of planar SOFC stack cell models: (a) co-flow; (b) counter-flow; (c) cross-flow.

Table 1
Geometric, material, and basic model parameters for a planar SOFC cell using hydrogen fuel and air oxidant.

Parameters	Value
Anode thickness (μm)	750
Cathode thickness (μm)	50
Electrolyte thickness (μm)	10
Active cell size ($l_x \times l_y$, cm × cm)	10 × 10
Anode porosity	0.38
Anode tortuosity	3
Anode mean particle diameter (μm)	1
Cathode porosity	0.3
Cathode tortuosity	3
Cathode mean particle diameter (μm)	1
Cell temperature (°C)	700
Anode conductivity (S m^{-1})	$3.356 \times 10^4 \exp(1392/T)$
Cathode conductivity (S m^{-1})	$1.223 \times 10^4 \exp(-600/T)$
Electrolyte conductivity (S m^{-1})	$3.34 \times 10^4 \exp(-10{,}300/T)$
Diffusion volume of H_2 (m^3 mol^{-1})	7.07×10^{-6}
Diffusion volume of H_2O (m^3 mol^{-1})	12.7×10^{-6}
Diffusion volume of O_2 (m^3 mol^{-1})	16.6×10^{-6}
Diffusion volume of N_2 (m^3 mol^{-1})	17.9×10^{-6}
Molar mass of H_2 (kg mol^{-1})	2×10^{-3}
Molar mass of H_2O (kg mol^{-1})	18×10^{-3}
Molar mass of O_2 (kg mol^{-1})	32×10^{-3}
Molar mass of N_2 (kg mol^{-1})	28×10^{-3}
Permeability of anode (m^2)	7.93×10^{-16}
Permeability of cathode (m^2)	3.06×10^{-16}
Viscosity of fuel (Pa s)	2.8×10^{-5}
Viscosity of air (Pa s)	4×10^{-5}
Knudsen diffusion coefficient of H_2 (m^2 s^{-1})	4.37×10^{-4}
Knudsen diffusion coefficient of H_2O (m^2 s^{-1})	1.46×10^{-4}
Knudsen diffusion coefficient of O_2 (m^2 s^{-1})	7.64×10^{-5}
Knudsen diffusion coefficient of N_2 (m^2 s^{-1})	8.17×10^{-5}
Inlet fuel/air pressure, P_{atm} (Pa)	1.013×10^5
Hydrogen molar fraction in fuel	0.97
Hydrogen utilization	70%
Oxygen utilization	20%
Rib-electrode contact resistance (Ω cm^2)	0.05
Cell output voltage (V)	0.7

The overall cell performance depends on the operating cell potential and the output current. The operating cell potential (V_{cell}) can be formally expressed as [20]:

$$V_{cell} = E_0^0 - \eta_{ASR;a} - \eta_a^0 - \eta_{act;a} - \eta_{ohm;a} - \eta_{ohm;el} - \eta_{ohm;c} - \eta_{act;c} - \eta_c^0 - \eta_{ASR;c} \quad (1)$$

where E_0^0 is the Nernst potential when the partial pressure of H_2, H_2O and O_2 are all at 1 atm ($E_0^0 = 1.01$ V at 973 K or 700 °C), $\eta_{act;a}$ and $\eta_{act;c}$ are respectively the anode and cathode activation overpotentials, $\eta_{ohm;a}$, $\eta_{ohm;el}$ and $\eta_{ohm;c}$ the ohmic overpotentials in the anode, electrolyte and cathode, $\eta_{ASR;a}$ and $\eta_{ASR;c}$ the anode–rib and cathode–rib interface overpotentials due to the contact resistance at the material boundaries, η_a^0 and η_c^0 the anode and cathode concentration balance potentials. The concentration balance potentials are calculated as [20]:

$$\eta_a^0 = -\frac{RT}{2F}\ln\left(\frac{p_{H_2,a}}{p_{H_2O,a}}\right)|_{TPB} \quad (2a)$$

$$\eta_c^0 = -\frac{RT}{4F}\ln\left(\frac{P_{O_2,c}|_{TPB}}{1\ \text{atm}}\right) \quad (2b)$$

where R is the universal gas constant, T the temperature at Kelvin, F the Faraday constant, $p_{H_2,a}$, $p_{H_2O,a}$ and $p_{O_2,c|TPB}$ are the partial pressure of H_2, the partial pressure of H_2O at the anode TPB and the partial pressure of O_2 at the cathode TPB, respectively. The details of computing the other overpotential terms in Eq. (1) will be described later.

The average output current density of the SOFC cell may be calculated by

$$\bar{j} = \frac{1}{l_x \times l_y}\int_{x=0}^{l_x}\int_{y=0}^{l_y} j_z\ dx\,dy \quad (3)$$

where l_x (l_y) is the cell length along the x (y) direction, j_z is the z component of the current density flux vector (see Fig. 2 for the axes definition).

2.2. Gas transport in porous electrode

2.2.1. Governing equations

The mass transport processes in porous electrodes are governed by the mass diffusion and convective equations. For species i, the transport equation can be expressed by [24]

$$\nabla \cdot N_i = \nabla \cdot (-D_i \nabla c_i + c_i u) = R_i \quad (4)$$

where D_i, c_i, and R_i are respectively the diffusion coefficient, molar concentration and reaction rate of species i, u the velocity of the mixture flow and $N_i = -D_i \nabla c_i + c_i u$ the total molar flux of species i. D_i and u may be obtained from the dusty gas model as described below.

2.2.2. Dusty gas model

The original dusty gas model in binary gas can be expressed [25–27]

$$\frac{N_1}{D_{1K}^{eff}} + \frac{x_2 N_1 - x_1 N_2}{D_{12}^{eff}} = -\frac{1}{RT}\left(p\nabla x_1 + x_1 \nabla p + x_1 \nabla p \frac{kp}{D_{1K}^{eff}\mu}\right) \quad (5a)$$

$$\frac{N_2}{D_{2K}^{eff}} + \frac{x_1 N_2 - x_2 N_1}{D_{12}^{eff}} = -\frac{1}{RT}\left(p\nabla x_2 + x_2 \nabla p + x_2 \nabla p \frac{kp}{D_{2K}^{eff}\mu}\right) \quad (5b)$$

where x_i is the molar fraction ($x_i = c_i/\sum_j c_j$), k the permittivity, μ the viscosity, p the total gas pressure, $D_{iK}^{eff}(=\varepsilon D_{iK}/\tau)$ the effective Knudsen diffusion coefficients and $D_{ij}^{eff}(=\varepsilon D_{ij}/\tau)$ the effective binary diffusion coefficients, $D_{ij}(= 3.198 \times 10^{-8} \times (T^{1.75}/(p(v_i^{1/3} + v_j^{1/3})^2))[(1/M_i) + (1/M_j)]^{1/2})$ the binary diffusion coefficient, ε, τ, v_i and M_i the porosity, tortuosity, diffusion volume and molar mass of species i, respectively [28,29]. The required parameters are shown in Table 1.

Summing both sides of eq.5a and eq.5b and using $x_1 + x_2 = 1$ and $\nabla x_1 = -\nabla x_2$, one gets

$$\frac{N_2}{D_{2K}^{eff}} = -\frac{N_1}{D_{1K}^{eff}} - \frac{\nabla p}{RT}\left(1 + \frac{kp}{\mu}\left(\frac{x_1}{D_{1K}^{eff}} + \frac{x_2}{D_{2K}^{eff}}\right)\right) \quad (6)$$

Substituting Eq. (6) into Eq. (5) yields

$$\begin{aligned} N_1 &= -\frac{D_{12}^{eff} D_{1K}^{eff}}{D_{12}^{eff} + x_1 D_{2K}^{eff} + x_2 D_{1K}^{eff}}\nabla c_1 \\ &\quad - \frac{D_{1K}^{eff} D_{2K}^{eff}}{D_{12}^{eff} + x_1 D_{2K}^{eff} + x_2 D_{1K}^{eff}}\frac{x_1 \nabla p}{RT} - \frac{c_1 k \nabla p}{\mu} \\ &= -\frac{D_{12}^{eff} D_{1K}^{eff}}{D_{12}^{eff} + x_1 D_{2K}^{eff} + x_2 D_{1K}^{eff}}\nabla c_1 \\ &\quad - c_1\left(\frac{D_{1K}^{eff} D_{2K}^{eff}}{RTc_{tot}\left(D_{12}^{eff} + x_1 D_{2K}^{eff} + x_2 D_{1K}^{eff}\right)} + \frac{k}{\mu}\right)\nabla p \\ &= N_1^{diffusion} + N_1^{convective} \end{aligned} \quad (7)$$

Therefore, the effective diffusion coefficients of the species are

$$D_1 = \frac{D_{12}^{eff} D_{1K}^{eff}}{D_{12}^{eff} + x_1 D_{2K}^{eff} + x_2 D_{1K}^{eff}} \quad (8a)$$

$$D_2 = \frac{D_{12}^{eff} D_{2K}^{eff}}{D_{12}^{eff} + x_1 D_{2K}^{eff} + x_2 D_{1K}^{eff}} \quad (8b)$$

The effective molar flow velocity is given by

$$u = -\left(\frac{D_{1K}^{eff} D_{2K}^{eff}}{RTc_{tot}\left(D_{12}^{eff} + x_1 D_{2K}^{eff} + x_2 D_{1K}^{eff}\right)} + \frac{k}{\mu}\right)\nabla p \quad (9)$$

where the $-(k/\mu)\nabla p$ term corresponds to the result by the usual Darcy's law [7,20].

2.3. Electrical conduction

The electronic charge transport in the electrodes and the ionic charge transfer in the electrolyte are governed respectively by

$$-\nabla \cdot (\sigma_e \nabla V_e) = 0 \quad (10a)$$

$$-\nabla \cdot (\sigma_i \nabla V_i) = 0 \quad (10b)$$

where σ_e (σ_i) is the electronic (ionic) conductivity of the electrode (electrolyte), V_e (V_i) the electric potential in the electrode (electrolyte). $-\sigma_e \nabla V_e (-\sigma_i \nabla V_i)$ is the flux vector of the electronic (ionic) current density. The electronic and ionic potential differences along the electrical current flux paths yield the ohmic overpotentials, $\eta_{ohm;a}$, $\eta_{ohm;c}$ and $\eta_{ohm;el}$.

The electric potential loss inside the interconnect plate is assumed to be negligible due to the high conductivity of the metallic material. The local current densities cross the interconnect/anode ($j_{I\to a}$) and the cathode/interconnect ($j_{c\to I}$) interfaces are determined by the associated electric potential changes, or the interface overpotentials:

$$j_{I\to a} = \frac{V_{e,I/a} - V_{e,a/I}}{ASR_{contact}} = \frac{\eta_{ASR;a}}{ASR_{contact}} \quad (11a)$$

$$j_{c\to I} = \frac{V_{e,c/I} - V_{e,I/c}}{ASR_{contact}} = \frac{\eta_{ASR;c}}{ASR_{contact}} \quad (11b)$$

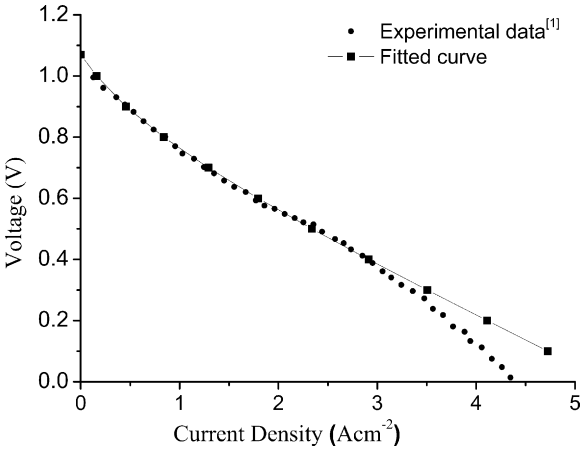

Fig. 3. Comparison of the experimental and theoretical *I–V* curves.

where $V_{e,l/a}$ and $V_{e,a/l}$ are respectively the interconnect and anode electric potentials at the anode–interconnect boundary, $V_{e,c/l}$ and $V_{e,l/c}$ the cathode and interconnect electric potentials at the cathode–interconnect boundary, $ASR_{contact}$ the area specific contact resistance.

2.4. Electrochemistry reaction

The current densities generated by the electrochemical reactions at the anode and cathode TPBs are described by the empirical Butler–Volmer equation as [14,27,30,31]

$$j_a = \begin{cases} j_{0,a}\left(\dfrac{p_{H_2,TPB}}{p_{H_2,f}}\right)^{0.11}\left(\dfrac{p_{H_2O,TPB}}{p_{H_2O,f}}\right)^{0.67}\left[\exp\left(\dfrac{2F\eta_{act,a}}{RT}\right)-\exp\left(\dfrac{-F\eta_{act,a}}{RT}\right)\right] & \text{for } p_{H_2O,TPB} < 14,000\,\text{Pa} \\ j_{0,a}\left(\dfrac{p_{H_2,TPB}}{p_{H_2,f}}\right)^{0.11}\left(\dfrac{14,000}{p_{H_2O,f}}\right)^{0.67}\left[\exp\left(\dfrac{2F\eta_{act,a}}{RT}\right)-\exp\left(\dfrac{-F\eta_{act,a}}{RT}\right)\right] & \text{for } p_{H_2O,TPB} \geq 14,000\,\text{Pa} \end{cases} \quad (12a)$$

$$j_c = j_{0,c}\left(\frac{p_{O_2,TPB}}{p_{O_2,air}}\right)^{1/2}\left[\exp\left(\frac{2F\eta_{act,c}}{RT}\right)-\exp\left(\frac{-2F\eta_{act,c}}{RT}\right)\right] \quad (12b)$$

where $j_{0,a}$ and $j_{0,c}$ are respectively the anode and cathode exchange current densities and may be determined by fitting the experimental *I–V* curves of button cells. Fitting the experiment of Ref. [1] for the temperature of 700 °C gives $j_{0,a} = 4280\,A\,m^{-2}$ and $j_{0,c} = 1070\,A\,m^{-2}$ (a hydrogen molar fraction of 0.9 in fuel was used in the fitting as deduced from the experimental open circuit voltage). As shown in Fig. 3, the theoretical *I–V* curve agrees with the experiment very well when the output current density is less than $3\,A\,cm^{-2}$ and is sufficient for practical applications. Notice that the exchange current densities may be temperature dependent [32], however, the temperature dependence is not a concern here as we are dealing with isothermal models.

The activation polarizations in Eq. (12), $\eta_{act;a}$ and $\eta_{act;c}$, are related to the electric and balance potentials by

$$\eta_{act;a} = V_{e,a/el} - V_{i,el/a} - \eta_a^0 \quad (13a)$$

$$\eta_{act;c} = V_{i,el/c} - V_{e,c/el} - \eta_c^0 \quad (13b)$$

where $V_{e,a/el}$ and $V_{i,el/a}$ are respectively the anode and electrolyte electric potentials at the anode–electrolyte boundary, $V_{i,el/c}$ and $V_{e,c/el}$ the electrolyte and cathode electric potentials at the cathode–electrolyte boundary.

2.5. Numerical method

Based on the observation that the coupling between the gas channel flows and the above described physical processes is weak [17], only the anode, electrolyte and cathode domains are included in the physical model that is assumed to be isothermal at the present. The gas channel flows and the interconnect ribs can be replaced with proper boundary conditions for gas transport and electric conduction [20]. For simplicity, the channels (ribs) on the anode-side and on the cathode-side are of the same width. As the TPBs are effective only at the region very close to the electrode/electrolyte interfaces [1], the TPBs are assumed to be located only at the electrode/electrolyte interfaces and there are no electrochemical reactions inside the electrodes.

Symmetries are used to reduce the model size and enhance numerical efficiency whenever possible. For co- and counter-flow designs, a multiple-channel cell of the size of $l_x \times l_y \times l_z$ (x: the fuel channel flow direction) may be represented by a single channel portion of the size of $l_x \times d_{pitch} \times l_z$, where d_{pitch} is the pitch width and $d_{pitch} = d_{channel} + d_{rib}$. Here $d_{channel}$ and d_{rib} are one half of the channel width and one half of the interconnect rib width, respectively. The reduction is significant as l_y in our model is 10 cm, while d_{pitch} is only a few millimeters.

2.5.1. Boundary conditions (BCs)

The boundary settings for the mass transport equations are shown in Table 2. The molar concentrations at the channel/anode or channel/cathode interface, c^0, c^0, c^0, and c^0, are related to the molar fractions by the ideal gas equation of state. The total gas pressure at the electrode/channel interface is set at 1 atm. As the overall results of the gas transports in porous electrodes are not very sensitive to the details of the channel flows [17,19,20], a linearly distributed hydrogen/oxygen concentration along the flow is specified on the channel/electrode boundary based on the fuel/oxygen utilization. For co-flow, both c^0 and c^0 decrease with x. For counter-flow, c^0 decreases with x while c^0 increases with x.

There is no apparent symmetry in a cross-flow design that can be used to simplify the model and different fuel channels correspond to different c^0. Multi-physics modeling of the whole cell can be memory and CPU demanding. Fortunately, excessive oxidant is used and the oxygen utilization is usually low in practical applications [17,19], i.e., c^0 does not vary widely over the whole cell. The overall cell performance may be approximately represented by a single fuel channel pitch with the average c^0 for the boundary condition of the air channels (an oxygen molar fraction of 0.19 is used in this work and corresponds to the oxygen utilization of 20%). Note that all air channels and cathode ribs are presented in this simplified model, but their length is d_{pitch} instead of l_y.

The contact resistance is set on the interface between interconnect ribs and the electrodes. The area specific contact resistances at the anode/interconnect and the cathode/interconnect boundaries are assumed to be uniform. The boundary settings for the electronic and ionic charge transfer equations are shown in Table 3. Due to the model difference, the distribution of electrical boundaries of the cross-flow design is also different from that of the co- or counter-flow design.

Table 2
Boundary settings for mass transports in electrodes.

Boundary	Anode/channel interface		Anode TPB		All others
BC type	(H_2) molar concentration	(H_2O) molar concentration	(H_2) Inward molar flux	(H_2O) Inward molar flux	Insulation/symmetry
BC	c^0	c^0	$-j_a/2/F$	$j_a/2/F$	
Boundary	Cathode/channel interface		Cathode TPB		All others
BC type	(O_2) molar concentration	(N_2) molar concentration	(O_2) Inward molar flux	(N_2) Inward molar flux	Insulation/symmetry
BC	c^0	c^0	$-j_c/4/F$	0	

Table 3
Boundary settings for the electronic and ionic charge transfer equations.

	Boundary BC type	Rib/cathode interface Reference potential	Rib/anode interface Reference potential	Cathode TPB Inward current flow	Anode TPB Inward current flow	All others Electric insulation
Electronic	BC	$V_{cell} - E_0^0$	0	j_c	$-j_a$	
Ionic	BC			$-j_c$	j_a	

2.5.2. Geometric model transformation

An anode-supported SOFC often consists of widely different geometric dimensions. As indicated in Table 1, the typical electrolyte thickness is in the order of 10 μm, while the cell size is about 10 cm × 10 cm. To be numerically stable, the large difference in model dimensions may require a mesh with a great number of degrees of freedom. A reduced dimensional difference is desirable for improving the numerical efficiency. Based on analysis of the ionic conducting equation, here we propose a method that enlarges the electrolyte thickness by n folds with the corresponding change in the electrolyte conductivity to moderate the thin film effect in the meshing step and decreases the number of degrees of freedom.

As described above, the electrolyte only involves the partial differential equation (PDE) for the ionic current conduction and the associated boundary conditions. If the boundary conditions remain the same and the ionic current is equivalent when the thickness of the electrolyte layer is scaled, the same physics is ensured. This provides the basis for the mathematical transformation. When the thickness of the electrolyte layer thickness is enlarged by n folds while the x–y dimension remains unchanged, $x \to x' = x$, $y \to y' = y$, $z \to z' = nz$, the same current flux before and after the inhomogeneous scaling requires:

$$J'_x = \frac{J_x}{n}, \quad J'_y = \frac{J_y}{n}, \quad J'_z = J_z \tag{14}$$

Based on $J_x = -\sigma_x(\partial V/\partial x)$, $J_y = -\sigma_y(\partial V/\partial y)$, $J_z = -\sigma_z(\partial V/\partial z)$ and $V(x, y, z) = V'(x', y', z')$, it is easy to know that the ionic conductivity of the electrolyte should transform with the geometric scaling as

$$\sigma'_x = \frac{\sigma_x}{n}, \quad \sigma'_y = \frac{\sigma_y}{n}, \quad \sigma'_z = n\sigma_z \tag{15}$$

In our 3D modeling, the thickness of electrolyte is scaled from 10 μm to 100 μm, so the effective conductivity of the electrolyte is changed from isotropic (σ_{el}, σ_{el}, σ_{el}) to anisotropic ($\sigma_{el}/10$, $\sigma_{el}/10$, $10\sigma_{el}$).

The above mathematical analysis is in principle general and applicable to other material components of the SOFC model and other geometric scaling and can efficiently decrease the mesh node numbers and enhance the efficiency of numerical simulation. Notice, however, the physics remains correct only if all the mathematical equations and the boundary conditions associated with the scaling transformation are considered properly.

2.5.3. Meshes and solutions

The finite element commercial software COMSOL MULTIPHSICS® Version 3.4 [24] is used in the present study to solve the PDEs with the appropriate boundary settings. The COMSOL stationary nonlinear solver uses an affine invariant form of the damped Newton method [24] to solve the discretized PDEs with a relative convergence tolerance of 1×10^{-6}. Tetrahedral meshes were used in the 3D models. For the co-flow and counter-flow models and with a pitch width of 2 mm (consists of a channel width of 1.2 mm and rib width of 0.8 mm), the number of mesh elements is 20698 and the number of degrees of freedom is 96940. The model geometry for the cross-flow design is quite complicated. For a pitch width of 2 mm, for example, there are 50 pairs of air channels and ribs in the model with a 10 cm fuel channel. To reduce the computational cost, the 10 cm fuel channel model is subdivided into five sub-models each with a fuel channel length of 2 cm. The fuel concentration boundary conditions for the sub-models are determined based on the assumed linear variation description. The results for the five sub-models are then combined to produce the results for the whole model. For a pitch width of 2 mm, the number of mesh elements is 44383 and the number of degrees of freedom is 209794 for each cross-flow sub-model.

3. Results and discussion

As examples of applications, the above described models are used to simulate the stack cell performance and optimize the rib design, providing the 3D distributions of physical quantities that are unavailable with 2D models and testing the validity of the rib design optimizations by 2D models.

3.1. Distributions of physical quantities

The distributions of physical quantities such as the hydrogen and oxygen molar fractions, current density and electrical potential in a stack cell are important information for the evaluation of a stack design. The following results are obtained with the basic model parameters listed in Table 1 and the stack cell assembly of a pitch width of 2 mm, with 1.2 mm for the channel width and 0.8 mm for the rib width. Due to the dimensional difference in the cell geometry, most plots use unequal axis scales.

3.1.1. Co- and counter-flow models

Both the co- and counter-flow stack cells produce the same total current corresponding to an average current density of 0.387 A cm^{-2} for the MEA. It is interesting to note that the average current density obtained by the present 3D model is identical to that obtained by a previous 2D model with the same model parameters [20], supporting the usefulness of a 2D modeling in this regard. The 3D distributions of physical quantities for the co-flow design are shown in Fig. 4. The distributions of physical quantities

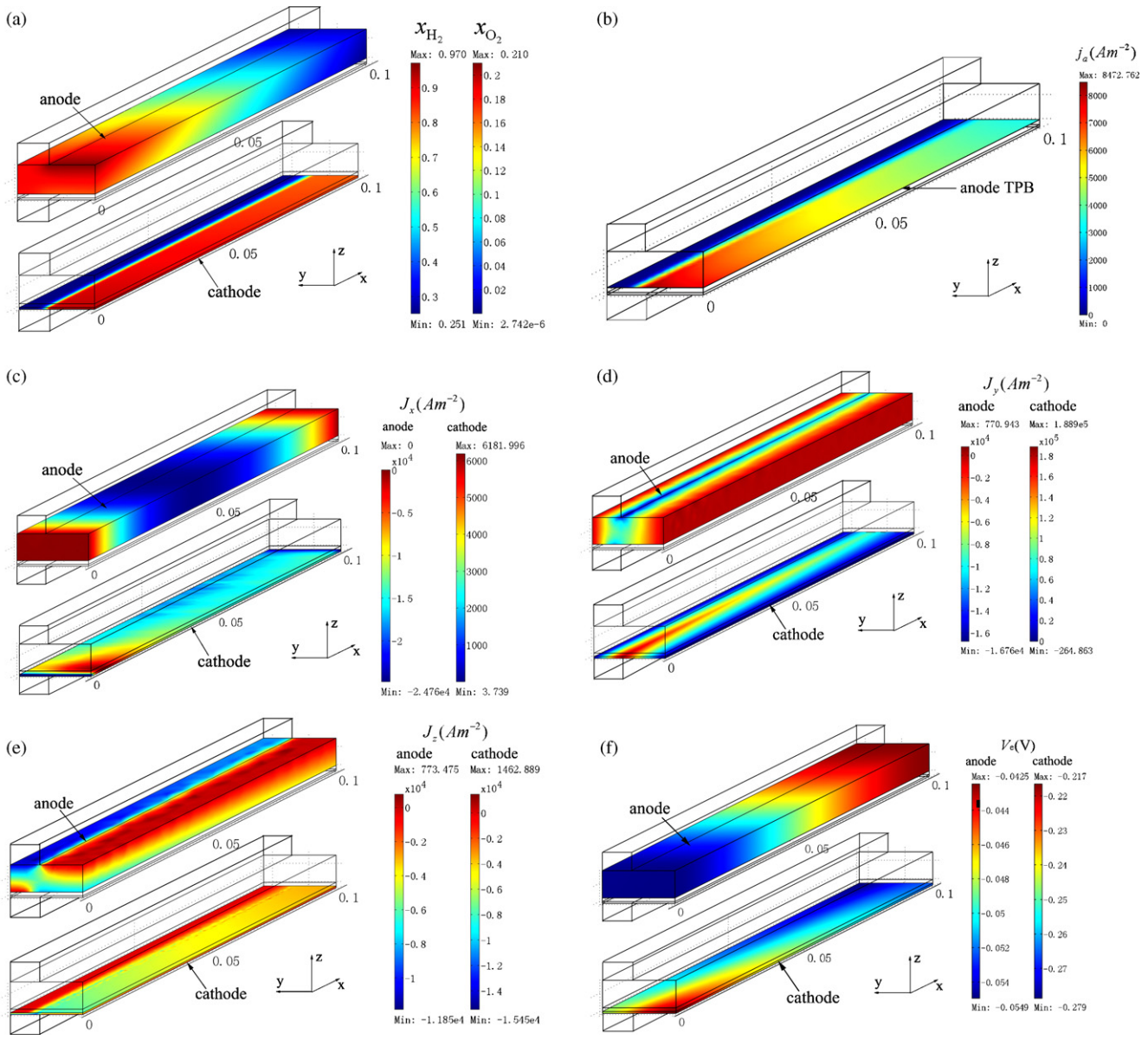

Fig. 4. The distributions of physical quantities for the co-flow cell: (a) hydrogen and oxygen molar fractions; (b) anode TPB current density by electrochemical reaction; (c) x component of the current density flux; (d) y component of the current density flux; (e) z component of the current density flux; (f) the electric potential.

for the counter-flow design are characteristically the same and are not shown.

The distributions of the hydrogen molar fraction on the anode and oxygen molar fraction on the cathode are shown in Fig. 4a. As can be seen from Fig. 4a, the hydrogen molar fraction at the anode TPB is similar for both the area under the fuel channel and the area under the interconnect rib. The oxygen molar fraction at the cathode TPB is, however, strongly affected by the rib presence. Except for the region very close to the rib-channel boundary, there is virtually no oxygen in the area under the rib. The H_2 and O_2 distributions for a 2D (y–z) cross-section of a given x in the 3D model and the underlying mechanism are basically the same as the previous 2D modeling results [20]. The 3D results, however, have the definite advantage of showing clearly the variations of H_2 and O_2 distributions along the flow direction.

Fig. 4b shows the current density distribution at the anode TPB generated by the electrochemical reactions that is affected by both the H_2 and O_2 distributions. Along the y-direction, the TPB current density is dominated by the O_2 distribution and there is basically no current generation for the area under the rib. For the area under the channel, the TPB current density profile is mainly determined by the H_2 distribution along the x-direction as the variation of the O_2 distribution is relatively small.

Fig. 4c–f shows the distributions of current density flux and electrical potential on the electrodes. The current density distributions show very interesting features. Although only the z component of the current density flux at the electrode–rib interface is responsible for producing the useful output current, the x and y components of the current density flux are of comparable or even larger magnitude. The y component of the current density flux is necessary for collecting by the rib the current generated under the channel area. The magnitude of the y component of the current density flux can be very large due to that the electrode layers are thin and the cross-section area for the y-component flux is small. The x component of the current density flux, which is ignored in a 2D model, is opposite to the fuel flow direction in the anode side, but is along the fuel flow direction in the cathode side. The magnitude of the x component of the current density flux can also be large and is larger than 2 A cm^{-2}

Table 4
Average output current densities ($\bar{j}$) for the five segments of the cross-flow models. x^0 is the H_2 molar fraction at the channel–anode interface boundary.

$x^0_{H_2}$	0.97–0.834	0.834–0.698	0.698–0.562	0.562–0.426	0.426–0.29
$\bar{j}$ (A cm^{-2})	0.482	0.421	0.376	0.337	0.298

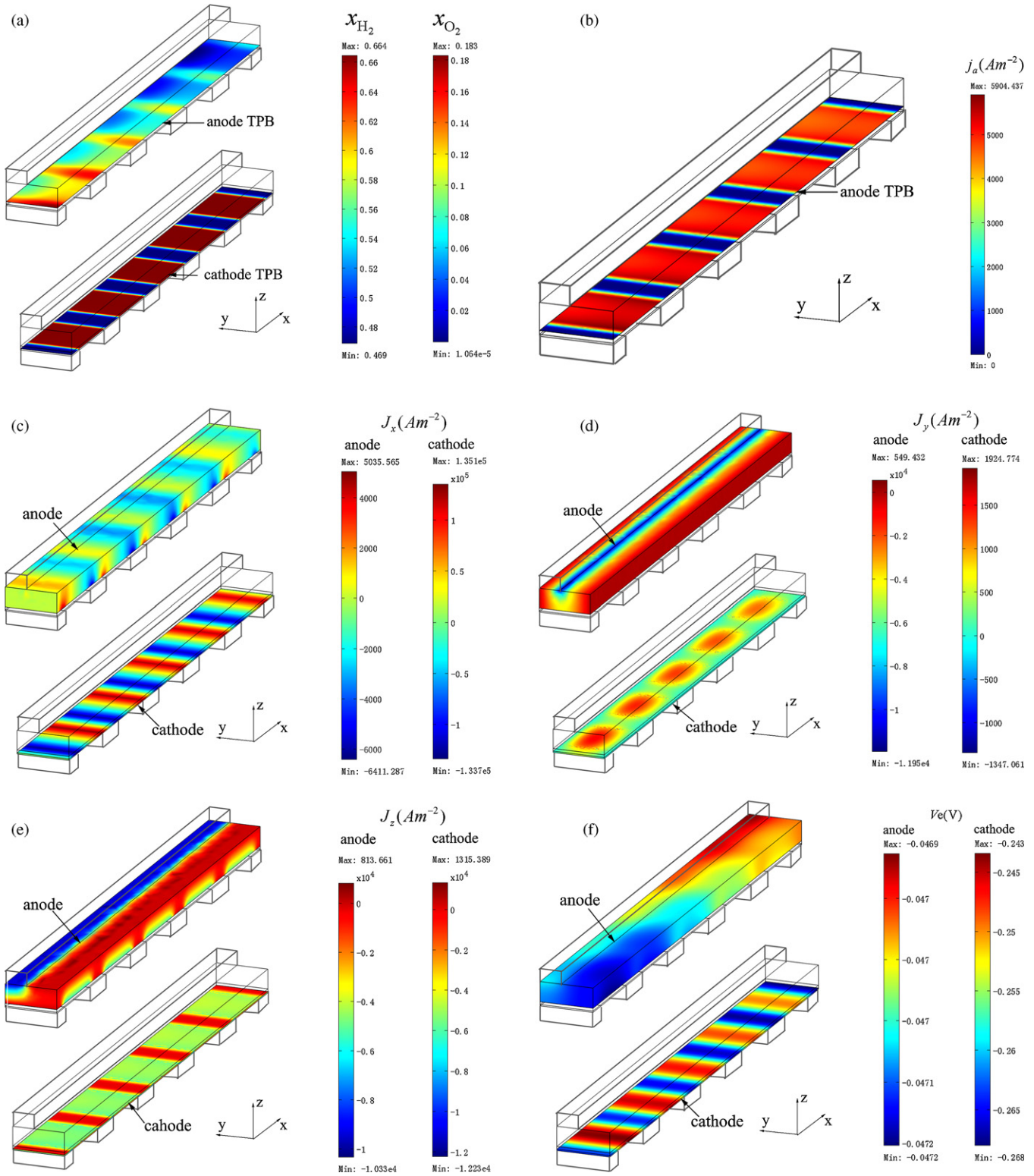

Fig. 5. The distributions of physical quantities for the cross-flow cell: (a) hydrogen and oxygen molar fractions at the TPBs; (b) anode TPB current density by electrochemical reaction; (c) *x* component of the current density flux; (d) *y* component of the current density flux; (e) *z* component of the current density flux; (f) the electric potential.

in the middle of anode. The profile of the current density flux can be explained by the distribution of the electric potential on the electrodes shown in Fig. 4f. For example, the difference of the electric potential between the fuel inlet and outlet is about −0.01 V and the electric conductivity of anode is about 1.4×10^5 S m^{-1} at 700 °C, consequently the average anode current density along the fuel flow direction is about $\bar{J}_x = \Delta V/R \approx -0.01\ V/(0.1\ \text{m}/1.4 \times 10^5\ \text{S m}^{-1}) = -1.4\ \text{A cm}^{-2}$, agreeing with the data shown in Fig. 4c. In fact, the electric potential distribution is also affected by the current density distribution, with the *z* component of the current density flux playing the dominant role. The anode electrical potential at the anode–rib interface is determined by the ohmic polarization due to the contact resistance (Eq. (11a)). As the *z* component of the current density at the anode–rib interface is higher for the fuel inlet than for the fuel outlet due to the hydrogen distribution (Fig. 4a and e), the electric potential at the fuel inlet is lower than that at the fuel outlet, causing the above described current flow along the *x* direction. In this sense, the *x* component of the current flux is determined by the *z* component of the current flux.

3.1.2. Cross-flow model

As described in Section 2.5.3, the whole cross-flow model is simulated with five sub-models each with a fuel channel length of 2 cm and an average O_2 molar fraction of 0.19 for the air channel. The pitch width is also 2 mm, 1.2 mm for the channel width and 0.8 mm for the rib width. The obtained average current densities for the five sub-models are shown in Table 4. The overall average current density for the cross-flow model is 0.383 A cm^{-2}, about 1% smaller than the result for the co- or counter-flow model.

The distributions of representative physical quantities for the cross-flow design are shown in Fig. 5. The 2D distributions of the hydrogen molar fraction on the anode TPB and oxygen molar fraction on the cathode TPB are shown in Fig. 5a. The distribution of oxygen molar fraction at the cathode TPB for the cross-flow design is characteristically the same as that for the co-flow design, with abundant oxygen for area under the air channel and almost no oxygen for area under the cathode rib. Similarly, the distribution of the anode TPB current density (Fig. 5b) is mainly determined by the distribution of oxygen molar fraction at the cathode TPB due to that the low ionic conductivity of the electrolyte requires the oxygen ions to move along almost the shortest possible paths in the electrolyte in order to minimize the ohmic polarization. This is the main reason for the very similar overall current outputs for the co- and cross-flow designs even though the distributions of other physical quantities such as the hydrogen molar fractions may appear to be very different for the co-flow and cross-flow designs.

As shown in Fig. 5a, the hydrogen molar fraction distribution on the anode TPB for the cross-flow cell exhibits interesting features and is characteristically different from that for the co-flow cell. The main tendency of the H_2 distribution on the anode TPB is to decrease along the flow direction, but the profile shows local maxima and is completely different from the linear pattern set on the channel/anode interface. This is in fact due to that the amount of hydrogen received at the TPB region has good correspondence with the H_2 distribution in the fuel channel (similar to that shown in Fig. 4a), but the H_2 consumption by the small current generation at the anode TPB regions shadowed by the cathode ribs is small, leaving the unconsumed hydrogen to form local maxima in the corresponding areas.

Fig. 5c–f shows the 3D distributions of the *x*, *y*, and *z* components of the current density flux and the electrical potential on the electrodes. Like the H_2 distribution on the anode TPB, the distributions of the current density flux and the electrical potential for the cross-flow may appear to be quite different from that for the co-flow. However, the distributions of the current flux and electrical potential for the cross-flow may also be easily understood like the H_2 distribution for the cross-flow. The mechanism behind the distributions of the current flux and electrical potential for the cross-flow cell is in principle the same as that described above for the co-flow cell, namely the H_2/O_2 and TPB current density distributions, the current collections by the ribs and the balance of the electrical potential, and is not repeated here.

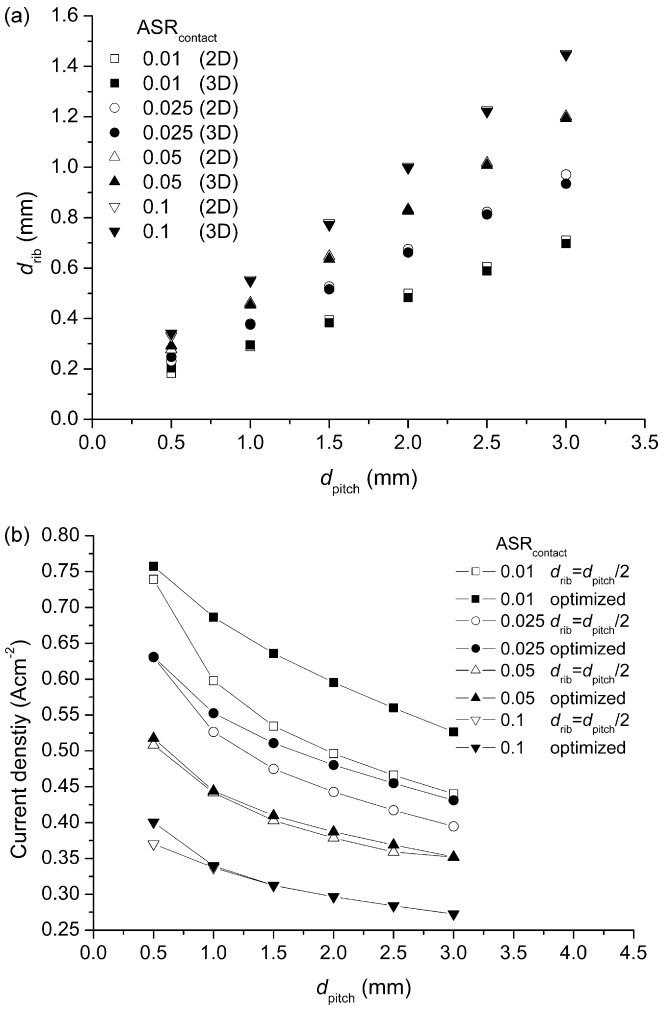

Fig. 6. Results of the rib width optimizations by 3D co-flow models: (a) comparison of the optimized rib widths with the 3D and 2D models; (b) the output current densities for the optimal rib width and for $d_{\text{rib}} = d_{\text{pitch}}/2$.

3.2. Rib width optimizations in 3D models

A series of calculations based on 2D models with the same basic model parameters listed in Table 1 have been performed for finding the optimal rib widths for given pitch sizes. The optimal rib widths were found by the 2D models to be dependent on the pitch widths linearly (but not proportionally), $d_{\text{rib}} = A + B \times d_{\text{pitch}}$, and the parameters in the linear relationship, *A* and *B*, depended practically only on the contact resistance at the electrode–rib interface [20]. Here we perform similar calculations with the 3D models to test the validity of the 2D modeling results.

3.2.1. Co- and counter-flow models

The results of the rib width optimizations for the co- and counter-flow designs are practically the same and only the results for the co-flow are discussed here. The optimization results with the 3D models for a few representative contact resistances are compared with the 2D results and shown in Fig. 6a. As can be seen, the

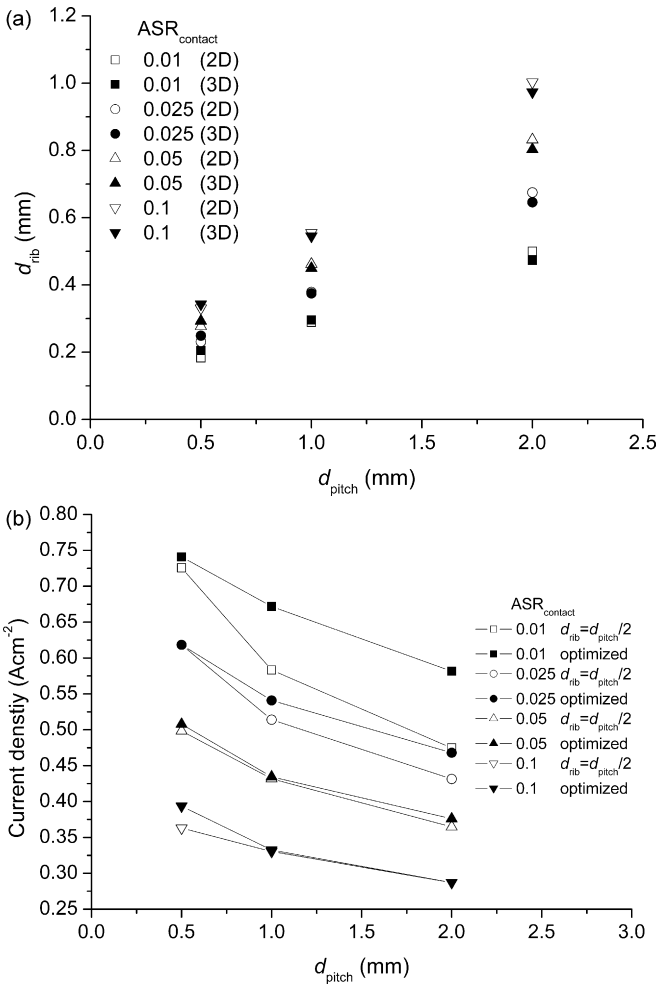

Fig. 7. Results of the rib width optimizations by 3D cross-flow models: (a) comparison of the optimized rib widths with the 3D and 2D models; (b) the output current densities for the optimal rib width and for $d_{rib} = d_{pitch}/2$.

results by the 2D and 3D models are quite similar. This is in fact not surprising as the 2D model can be viewed as a cross section in the 3D model and the variation of the H_2 concentration in the fuel channel in the 3D model may be well approximated with the average H_2 concentration used in the 2D model due to the weak dependence of the optimal rib width on the H_2 concentration [20]. The nearly identical optimization results by the 2D and 3D models also produce nearly identical optimal output current densities. To illustrate the benefit of the rib optimization, the optimal current densities are compared with that of a naïve design of $d_{rib} = d_{pitch}/2$ in Fig. 6b. When the contact resistance is small and $d_{pitch} \geq 2$ mm, the optimal output current densities are 10–20% larger than the naïve design. When the contact resistance is relatively large, the benefit of the rib optimization over the naïve design is not obvious as the naïve design is close to be optimal.

3.2.2. Cross-flow model

The geometry and the distributions of physical quantities in a cross-flow model are very different from that in a co-flow or counter-flow model, or that appeared in a 2D model. It may be rather questionable intuitively for a 2D model to be representative of a 3D cross-flow model. As shown in Fig. 7a, however, the results of the rib width optimizations by the 3D cross-flow model and the simplified 2D model are very close to each other. Similarly, the output current densities for the cross-flow cells shown in Fig. 7b are also close to that for the co-flow cells shown in Fig. 6b, though the

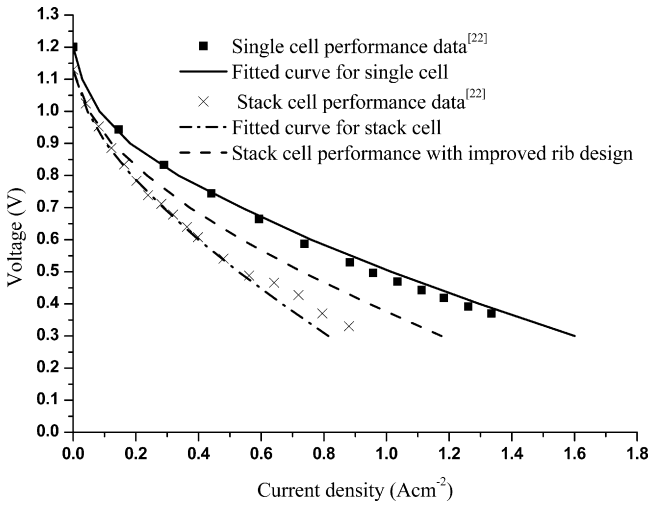

Fig. 8. Comparison of the theoretical and experimental *I–V* results. The difference between the dashed line and the dash-dotted line shows a possible performance improvement of the stack cell if a better rib-channel structure is used.

former may be 1–2% smaller than the latter. The ability of a simplified 2D model to represent a 3D cross-flow model is in fact not surprising due to the dominance of the effects of the cathode ribs on the TPB current generation and the inconsequential role of the anode ribs on the hydrogen transport and the TPB current generation, as described above in Section 3.1.2. The results are gratifying since the optimization modeling is important for improving the engineering design and the 2D modeling is much more economic than the 3D modeling.

3.2.3. Comparison with the experimental data

An example has been given in Fig. 3 to show that the theoretical model may reproduce the experimental *I–V* data by adjusting the anode and cathode exchange current densities that are dependent on a variety of microstructural parameters [15]. The theoretical model is further used here to explain the different *I–V* results of a single cell and an identical cell in a three-cell stack observed experimentally [22]. As shown in Ref. [14], the current collector of platinum mesh used in the single cell testing [22] may be described by model parameters of $d_{pitch} = 0.3$ mm, $d_{rib} = 0.05$ mm and $ASR_{contact} = 0.008\ \Omega\,cm^2$. Fig. 8 shows the comparison of the experimental data of Ref. [22] for the temperature of 700 °C and the theoretical results with $j_{0,a} = 400\ A\,m^{-2}$ and $j_{0,c} = 100\ A\,m^{-2}$ (based on the experimental open circuit voltage of 1.2 V, a hydrogen molar fraction of 0.996 in the input fuel was used in the fitting, correlating well with the pure hydrogen fuel used in the experiment). As shown in Fig. 8, the agreement between the theoretical and experimental *I–V* curves is satisfactory.

The experimental three-cell stack consists of five rib-channel pitches in a square cell of 5 cm × 5 cm [22], corresponding to $d_{pitch} = 5$ mm and $d_{rib} = 0.7$ mm in the theoretical model. The input fuel flow rate may be deduced from the fuel utilization for a given output current density stated in the experiment [22]. Based on these data, the theoretical performance of a single cell in the three-cell stack may be obtained and shown together with experimental results in Fig. 8. Notice that the experimental current densities in Ref. [22] were scaled by a factor of 18.49/25 here as the fuel cell area used in the experimental presentation was 18.49 cm^2 instead of the actual 25 cm^2 used in this work. Clearly, the experimental observation of the decreased performance of a stack cell in comparison with the corresponding single cell is quantitatively explained by the theory, demonstrating the validity and the predictive power of the theoretical model.

Notice that the pitch width of 5 mm used in the experiment is unnecessarily large and detrimental to the stack cell performance [19]. If a pitch width of 2 mm and a rib width of 0.42 mm were used in the stack construction, the stack cell performance would be improved notably, as shown in Fig. 8. For example, the output current density of such a stack cell for the operating voltage of 0.7 V is expected to be 0.37 A cm^{-2}, an increase of about 30% over the result of 0.29 A cm^{-2} for the experimental stack cell.

4. Summary

We have presented three-dimensional multi-physics numerical models for planar SOFC cells with the co-, counter- and cross-flow stack designs. The models are capable of handling the electronic conduction in the electrodes, ionic conduction in the electrolyte, mass transport in the porous electrodes and electrochemical reactions on the three phase boundaries as well as the critical role of interconnect ribs on the cell performance. A geometric scaling algorithm that is in principle general is proposed to improve the meshing efficiency of the 3D model. Numerical examples for different flow designs are presented and the 3D distributions of physical quantities are displayed and analyzed with interesting features that are unavailable to the 2D models. The models are also used to find the optimal rib widths for given channel–rib pitch widths. The results by the 3D models show that the stack cell performances and the optimal rib widths are all very similar for co-, counter-, and cross-flow designs and can be well represented by the corresponding 2D models, simplifying the future modeling work as far as the cell current output and the rib optimization are concerned.

Acknowledgements

We gratefully acknowledge the financial support of the Knowledge Innovation Program and the Key Program of the Chinese Academy of Sciences (KJCX1.YW.07), the National High-tech R&D Program of China (2007AA05Z156) and the National Science Foundation of China (10574114).

References

[1] J.W. Kim, A.V. Virkar, K.Z. Fung, K. Mehta, S.C. Singhal, J. Electrochem. Soc. 146 (1999) 69–78.
[2] EG&G Technical Services, Inc., Fuel Cell Handbook, Seventh edition, 2004.
[3] F. Zhao, A.V. Virkar, J. Power Sources 141 (2005) 79–95.
[4] S.D. Kim, J.J. Lee, H. Moon, S.H. Hyun, J. Moon, J. Kim, H.W. Lee, J. Power Sources 169 (2007) 265–270.
[5] S.C. Singhal, K. Kendall, High Temperature Solid Oxide Fuel Cell: Fundamentals, Design, and Applications, Elsevier Advanced Technology, Oxford, 2003.
[6] S. Kakaç, A. Pramuanjaroenkij, X.Y. Zhou, Int. J. Hydrogen Energy 32 (2007) 761–786.
[7] R. Bove, S. Ubertini, J. Power Sources 19 (2006) 543–559.
[8] K. Tseronis, I.K. Kookos, C. Theodoropoulos, Chem. Eng. Sci. 63 (2008) 5626–5638.
[9] M. Ni, D.Y.C. Leung, M.K.H. Leung, Energy Convers. Manage. 50 (2009) 268–278.
[10] E.V. Tsipis, V.V. Kharton, J. Solid State Electrochem. 12 (2008) 1039–1060.
[11] V.M. Janardhanan, O. Deutschmann, Z. Phys. Chem. 221 (2007) 443–478.
[12] A. Pramuanjaroenkij, A. Kakaç, X.Y. Zhou, Int. J. Hydrogen Energy 33 (2008) 2547–2565.
[13] B. Kenney, K. Karan, Solid State Ionics 178 (2007) 297–306.
[14] D.H. Jeon, J.H. Nam, C.J. Kim, J. Electrochem. Soc. 153 (2) (2006) A406–A417.
[15] D. Chen, Z. Lin, H. Zhu, R.J. Kee, J. Power Sources 191 (2009) 240–252.
[16] K.P. Recknagle, R.E. Williford, L.A. Chick, D.R. Rector, M.A. Khaleel, J. Power Sources 113 (2003) 109–114.
[17] M.A. Khaleel, Z. Lin, P. Singh, W. Surdoval, D. Collins, J. Power Sources 130 (2004) 136–148.
[18] M.A. Khaleel, D.R. Rector, Z. Lin, K. Johnson, K.P. Recknagle, Int. J. Multiscale Comput. Eng. 3 (2005) 33–48.
[19] Z. Lin, J.W. Stevenson, M.A. Khaleel, J. Power Sources 117 (2003) 92–97.
[20] S. Liu, C. Song, Z. Lin, J. Power Sources 183 (2008) 214–225.
[21] W. Bi, D. Chen, Z. Lin, Int. J. Hydrogen Energy 34 (2009) 3873–3884.
[22] B.W. Chung, C.N. Chervin, J.J. Haslam, A.Q. Pham, R.S. Glass, J. Electrochem. Soc. 152 (2) (2005) A265–A269.
[23] H.Y. Jung, S.-H. Choi, H. Kim, J.-W. Son, J. Kim, H.-W. Lee, J.-H. Lee, J. Power Sources 159 (2006) 478–483.
[24] Comsol AB., Comsol Multiphysics® Version 3.4 User's Guide, 2007.
[25] R. Krishna, J.A. Wesselingh, Chem. Eng. Sci. 52 (1997) 861–991.
[26] R. Suwanwarangkul, E. Croiset, M.W. Fowler, P.L. Douglas, E. Entchev, M.A. Douglas, J. Power Sources 122 (2003) 9–18.
[27] R. Suwanwarangkul, E. Croiset, E. Entchev, S. Charojrochkul, M.D. Pritzker, M.W. Fowler, P.L. Douglas, S. Chewathanakup, H. Mahaudom, J. Power Sources 161 (2006) 308–322.
[28] E.N. Fuller, P.D. Schettler, J.C. Giddings, Ind. Eng. Chem. 58 (1966) 18–27.
[29] R.P. O'Hayre, S.W. Cha, W. Colella, F.B. Prinz, Fuel Cell Fundamentals, John Wiley & Sons, 2006, p. 144 & 153.
[30] A. Bieberle, L.P. Meier, L.J. Gauckler, J. Electrochem. Soc. 148 (6) (2001) A646–A656.
[31] P. Aguiar, C.S. Adjiman, N.P. Brandon, J. Power Sources 138 (2004) 120–136.
[32] H. Zhu, R.J. Kee, J. Electrochem. Soc. 155 (7) (2008) B715–B729.